Sun *et al. BMC Cancer* (2025) 25:1480
https://doi.org/10.1186/s12885-025-14806-5

BMC Cancer

RESEARCH Open Access

Radiomics analysis using machine learning to predict perineural invasion in pancreatic cancer

Yuan Sun[1†], Yan Li[1†], Ming Li[1], Tao Hu[1] and Jiangyu Wang[1*]

Abstract

Background Pancreatic cancer is one of the most aggressive and lethal malignancies of the digestive system and is characterized by an extremely low five-year survival rate. The perineural invasion (PNI) status in patients with pancreatic cancer is positively correlated with adverse prognoses, including overall survival and recurrence-free survival. Emerging radiomic methods can reveal subtle variations in tumor structure by analyzing preoperative contrast-enhanced computed tomography (CECT) imaging data. Therefore, we propose the development of a preoperative CECT-based radiomic model to predict the risk of PNI in patients with pancreatic cancer.

Patients and methods This study enrolled patients with pancreatic malignancies who underwent radical resection. Computerized tools were employed to extract radiomic features from tumor regions of interest (ROIs). The optimal radiomic features associated with PNI were selected to construct a radiomic score (RadScore). The model's reliability was comprehensively evaluated by integrating clinical and follow-up information, with SHapley Additive exPlanations (SHAP)-based visualization to interpret the decision-making processes.

Results A total of 167 patients with pancreatic malignancies were included. From the CECT images, 851 radiomic features were extracted, 22 of which were identified as most strongly correlated with PNI. These 22 features were evaluated using seven machine learning methods. We ultimately selected the Gaussian naive Bayes model, which demonstrated robust predictive performance in both the training and validation cohorts, and achieved area under the ROC curve (AUC) values of 0.899 and 0.813, respectively. Among the clinical features, maximum tumor diameter, CA-199 level, blood glucose concentration, and lymph node metastasis were found to be independent risk factors for PNI. The integrated model yielded AUCs of 0.945 (training cohort) and 0.881 (validation cohort). Decision curve analysis confirmed the clinical utility of the ensemble model to predict perineural invasion.

Conclusion The combined model integrating clinical and radiomic features exhibited excellent performance in predicting the probability of perineural invasion in patients with pancreatic cancer. This approach has significant potential to optimize therapeutic decision-making and prognostic evaluation in patients with PNI.

Keywords Pancreatic cancer, Perineural invasion, Radiomics, Contrast-enhanced computed tomography, Prediction model

---

[†]Yuan Sun and Yan Li share first authorship.

*Correspondence:
Jiangyu Wang
844816832@qq.com

Full list of author information is available at the end of the article

The contributions of this paper can be summarized in 6 chapters:

Chapter 1 begins by describing the theoretical dimensions of the research and the research status and significance. Chapter 2 presents the methodology used for this study. Chapter 3 presents the results of the research. Chapter 4 presents an analysis of the results and focus group discussions. Chapter 5 focuses on the Limitations of the study. Chapter 6 details the research conclusions.

Introduction

Pancreatic cancer is the most aggressive malignancy of the digestive system and ranks as the seventh leading cause of cancer-related mortality worldwide. Its insidious onset and nonspecific early symptoms contribute to delayed diagnosis, suboptimal therapeutic outcomes, and a dismal five-year survival rate of approximately 9% [1]. Pancreatic ductal adenocarcinoma (PDAC), the predominant histological subtype accounting for more than 90% of all pancreatic malignancies, is associated with a particularly poor prognosis. Although surgical resection is the primary curative option for PDAC and other pancreatic neoplasms, only 15–20% of patients are deemed eligible for surgery at the time of the initial diagnosis [2, 3]. Therefore, adjuvant therapies such as radiotherapy and chemotherapy are the primary forms of treatment in advanced cases [4]. These current circumstances underscore the urgent need for novel auxiliary diagnostic strategies to achieve early disease identification, thereby guiding therapeutic protocols and improving patient prognosis.

Perineural invasion (PNI), defined histologically as tumor cell infiltration along nerve bundles or within the epineurium, perineurium, or endoneurium, is a hallmark of aggressive biological behavior in multiple malignancies. It is strongly associated with early recurrence, reduced survival, and adverse prognostic outcomes [5–7]. Despite its clinical importance, the molecular mechanisms underlying PNI remain poorly understood, and targeted therapies are lacking. Current evidence suggests that the overexpression of membrane proteins such as CD74 and cadherins in pancreatic cancer cells is correlated with PNI progression and prognosis [8]. Dysregulation of cell cycle regulators, including cyclin D1, has also been implicated in the pathogenesis of PNI [9]. Furthermore, the intricate tumor microenvironment of pancreatic cancer facilitates PNI through interactions with Schwann cells, macrophages, T cells, stromal cells, and fibroblasts, which collectively promote neural invasion and poor outcomes [10]. Pathways such as MMP1/PAR1/SP/NK1R signaling have been shown to mediate neurotropic invasion in pancreatic cancer [11]. Molecular biomarkers focus primarily on exploring molecular mechanisms and pathways, but their heterogeneity precludes the development of universal assays applicable for clinical use. Clinically, PNI serves as an independent prognostic factor for reduced overall survival and disease-free survival [12, 13] and is strongly linked to postoperative neuropathic pain due to nerve sheath disruption and proinflammatory molecule secretion [14]. There are currently no specific biomarkers that accurately predict the probability of PNI occurrence. Therefore, early detection of PNI is critical to optimize clinical management.

Contrast-enhanced computed tomography (CECT) plays a pivotal role in pancreatic cancer diagnosis, surgical planning, and anatomical delineation [15]. Although Khristenko et al. reported that preoperative CECT can detect perineural invasion (PNI), its visual assessment is operator-dependent and nonquantitative, and may therefore miss subtle positive findings. Consequently, the diagnostic accuracy of extrapancreatic perineural invasion (EPNI) in pancreatic ductal adenocarcinoma (PDAC) is unclear [16]. Moreover, the absence of quantitative biomarkers for PNI prediction poses a significant clinical challenge. Radiomics—an emerging discipline involving high-throughput extraction of quantitative features from medical images—offers unprecedented opportunities to characterize pathological tissues and predict clinical outcomes [17]. Although Liu et al. demonstrated the value of machine learning (ML)-based radiomics to predict intrahepatic cholangiocarcinoma (ICC) [18], studies on PNI prediction in pancreatic cancer patients are scarce. Although Zou et al. developed a serum biomarker-based nomogram for PNI prediction [19], no studies to date have established an interpretable ML framework that integrates clinical-radiological characteristics with CT radiomics for predicting neural invasion in patients with pancreatic cancer.

The aim of this study is to develop and validate an ML algorithm that integrates textural features derived from radiomics with radiological and clinical parameters (e.g., blood glucose levels, CA19-9) to stratify PNI risk. By synthesizing imaging biomarkers and serum indicators associated with PNI, we propose a multimodal predictive framework to guide personalized therapeutic decision-making.

Principal Contributions:

- The first development of an interpretable ML-based noninvasive prediction model for pancreatic cancer neural invasion using clinical-radiological features and CT radiomics.
- A precision noninvasive preoperative PNI predictor was developed to guide nerve-sparing surgical planning. Risk stratification management system

for bridging imaging diagnosis with personalized therapy.
- Addressing critical research deficiencies in developing clinically applicable prediction systems for pancreatic cancer perineural invasion by ML.

Related work

With the advancements in computer technology and artificial intelligence, machine learning methods based on radiological images for predicting clinical outcomes have gained increasing traction. Current research has demonstrated that advanced algorithms such as convolutional neural networks and deep learning have matured considerably in identifying imaging features.

Marko Sarac et al. proposed a detail extraction pyramid network (DEPNet) as a robust computer-aided model for predicting COVID-19 infection cases from CT images in the COVID-CT-MD dataset. This model classifies COVID-19 cases against other respiratory diseases with 99.45% accuracy. It also precisely localizes lesion areas (primarily ground-glass opacities), aiding clinicians in visual diagnosis [20].

S. Prakash et al. introduced a novel hybrid wavelet filter for precise image enhancement with the aim to generate high-quality images to detect cancer. Specifically, the authors combined Gabor and Legendre filters. Edge detection employs the Canny operator for image smoothing. The Gabor-Legend filter (GLFIL) process produced superior enhanced images, which were subsequently classified using neural networks optimized via animal migration optimization. The proposed technique achieved 98% accuracy, outperforming existing algorithms [21].

Timea Bezdan et al. developed a hybrid elephant herd optimization-based approach to automatically search for near-optimal hyperparameters in CNNs. This method enables rapid and automated classification of glioma brain tumors from MRI scans and demonstrates significant superiority over comparative methods [22].

Zivkovic, M et al. created a hybrid arithmetic optimization algorithm (AOA) that integrates CNNs and XGBoost. By tuning XGBoost hyperparameters with this hybrid AOA, they achieved 99.39% COVID-19 detection accuracy using chest X-rays alone, and substantially optimized diagnostic costs and clinical accessibility [23].

These studies validate the clinical value of machine learning algorithms. Our research aims to integrate radiomic and clinical features through multimodal machine learning algorithms to accurately detect pancreatic cancer perineural invasion preoperatively, thereby guiding clinical decision-making.

Methods

This study was approved by the Ethics Committee of the First Affiliated Hospital of Chongqing Medical University and strictly adhered to the principles of the Declaration of Helsinki. The requirement for informed consent was waived for all participants.

A retrospective analysis was conducted on patients who underwent pancreatic cancer (PC) resection at our center. The surgical pathology records of PC patients who underwent resection between 2018 and 2024 were reviewed. All postoperative pathological results for PC patients were assessed by experienced pathologists blinded to the radiomics findings, with perineural invasion (PNI) defined as the presence of tumor cells within nerve bundles in R0-resected tumor specimens (Fig S1). Patients were included if they met the following criteria: (1) preoperative contrast-enhanced computed tomography (CECT) performed within 1 month before surgery, with complete surgical pathology reports; (2) age ≥ 18 years, having undergone radical pancreatic resection (including pancreaticoduodenectomy or distal pancreatectomy), with postoperative pathological confirmation of pancreatic ductal adenocarcinoma (PDAC); (3) availability of high-quality preoperative abdominal CECT scans (within 2–4 weeks before surgery) suitable for radiomics analysis; and (4) clear documentation or evaluability of perineural invasion (PNI) status in surgical pathology reports.

The exclusion criteria were as follows: (1) prior neoadjuvant radiotherapy, chemotherapy, or tumor-modifying therapies (e.g., radiofrequency ablation) before CECT; (2) the presence of other primary malignancies; (3) incomplete clinical data; and (4) severe CT artifacts or missing data preventing radiomic quantification.

Image acquisition

All CT scans were performed using multidetector CT scanners with multiphasic contrast-enhanced protocols. Tumor segmentation was conducted on portal venous phase images. The imaging parameters included a CECT matrix of 512 × 512 × 16, an automatic or variable tube current (85.8% [85/99] of the scans used 120 kV), and a slice thickness of 2.0–5.0 mm.

Data collection and radiomic feature extraction

DICOM-format abdominal CT images (512 × 512 resolution) were retrieved from the hospital's imaging database. Clinical data, including PNI status, maximum tumor diameter, CA19-9 levels, blood glucose concentration, and lymph node metastasis, were extracted from electronic medical records.

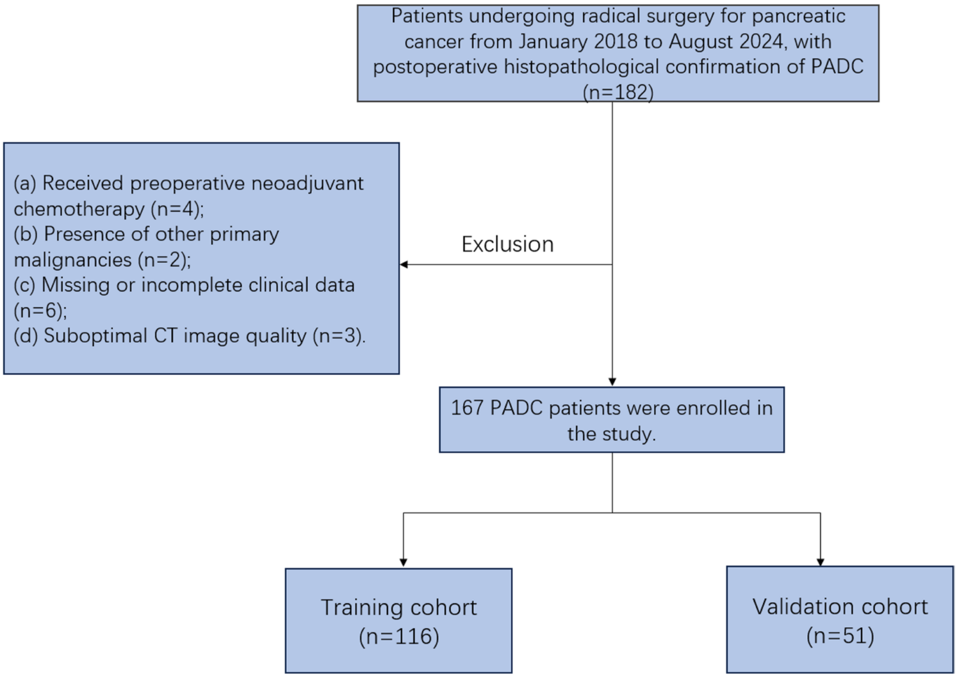

Fig. 1 The flowchart of pancreatic cancer case screening. (Random state=38, training cohort=116, validation cohort=51)

Segmentation and feature extractio

The tumor regions of interest (ROIs) were manually segmented using 3D Slicer software (version 5.7.0) by two radiologists (with 10 years of abdominal imaging experience) under the supervision of a senior radiologist. ROIs were delineated on arterial phase CT images (original 1 mm slice thickness), excluding necrotic areas, and validated via multiplanar reconstruction (MPR) (Fig. 1a). Vascular structures and bowel gas were excluded. Challenging cases were reviewed by a multidisciplinary team.

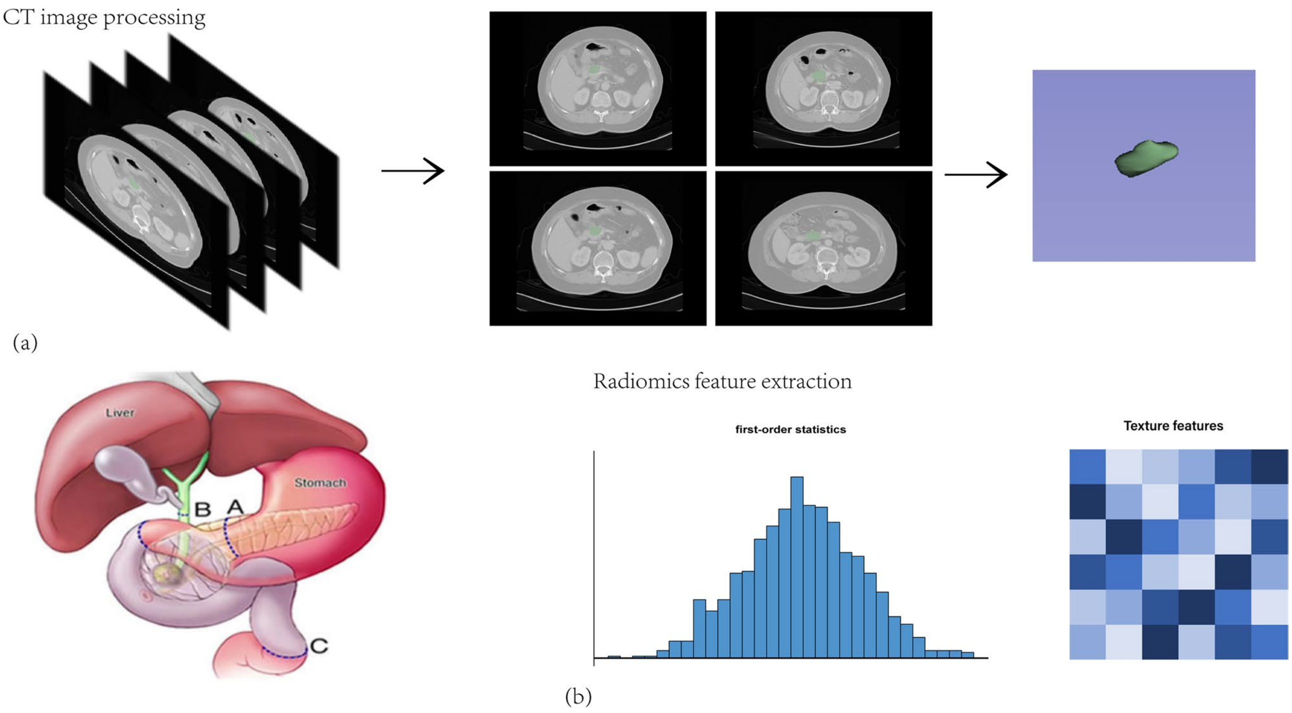

Fig. 2 (**a**) Flowchart of abdominal CT image segmentation and (**b**) feature extraction

Table 1 Baseline characteristics of the training and test cohorts

Variables	Training cohort (n = 116)	Validation cohort (n = 51)	p
PNI, n (%)			1
0	69 (59)	30 (59)	
1	47 (41)	21 (41)	
age, Mean ± SD	62.24 ± 9.25	60.94 ± 11.02	0.464
sex, n (%)			0.514
female	40 (34)	21 (41)	
male	76 (66)	30 (59)	
high, Median (Q1,Q3)	162 (157, 168)	165 (157.5, 168.5)	0.331
weight, Median (Q1,Q3)	59 (52.38, 65)	60 (50.55, 70.25)	0.535
bmi, Median (Q1,Q3)	22.15 (20.63, 24.13)	22.1 (20.4, 24)	0.946
sughistory, n (%)			0.755
0	84 (72)	35 (69)	
1	32 (28)	16 (31)	
othercancer, n (%)			0.071
0	114 (98)	47 (92)	
1	2 (2)	4 (8)	
hbp, n (%)			0.815
0	90 (78)	38 (75)	
1	26 (22)	13 (25)	
dm, n (%)			0.301
0	90 (78)	35 (69)	
1	26 (22)	16 (31)	
heartdisease, n (%)			1
0	109 (94)	48 (94)	
1	7 (6)	3 (6)	
lungdisease, n (%)			0.677
0	110 (95)	50 (98)	
1	6 (5)	1 (2)	
pancreatitishistory, n (%)			0.278
0	108 (93)	50 (98)	
1	8 (7)	1 (2)	
drink, n (%)			0.871
0	88 (76)	40 (78)	
1	28 (24)	11 (22)	
smoke, n (%)			1
0	78 (67)	35 (69)	
1	38 (33)	16 (31)	
NAHA, n (%)			0.452
I	6 (5)	2 (4)	
II	63 (54)	23 (45)	
III	47 (41)	26 (51)	
ASA, n (%)			0.73
I	14 (12)	7 (14)	
II	80 (69)	38 (75)	
III	20 (17)	6 (12)	
IV	2 (2)	0 (0)	
NLR, Median (Q1,Q3)	3.18 (2.34, 4.19)	2.98 (2.2, 4.06)	0.625
PLR, Median (Q1,Q3)	185.76 (141.16, 244.79)	176.58 (135.8, 232.55)	0.375
LMR, Median (Q1,Q3)	3.18 (2.34, 4.19)	2.98 (2.2, 4.06)	0.625
prognostic_nutritional_index, Mean ± SD	46.16 ± 5.71	45.35 ± 6.36	0.437
SII, Median (Q1,Q3)	708.12 (452.08, 1082.32)	586.29 (430.9, 1010.71)	0.318
preWBC, Median (Q1,Q3)	5.64 (4.65, 7.2)	5.76 (4.86, 6.72)	0.905

Table 1 (continued)

Variables	Training cohort (n = 116)	Validation cohort (n = 51)	p
prePLT, Median (Q1,Q3)	224.5 (177.75, 276)	209 (166, 257.5)	0.208
preNC, Median (Q1,Q3)	3.76 (2.99, 5.15)	3.65 (2.96, 4.8)	0.732
preLC, Median (Q1,Q3)	1.12 (0.94, 1.51)	1.27 (0.92, 1.46)	0.702
preMC, Median (Q1,Q3)	0.48 (0.36, 0.62)	0.42 (0.37, 0.54)	0.3
CA199, Median (Q1,Q3)	237.5 (78.22, 554.55)	191.7 (54.45, 399.25)	0.132
CEA, Median (Q1,Q3)	3.75 (2.38, 5.6)	3.1 (1.94, 4.35)	0.129
preHb, Mean ± SD	124.74 ± 17.55	122.86 ± 17.2	0.52
preAlb, Mean ± SD	39.92 ± 4.89	38.92 ± 4.96	0.231
preTB, Median (Q1,Q3)	72.95 (11.9, 146.3)	69.8 (13.5, 151.1)	0.714
preALT, Median (Q1,Q3)	70.5 (25, 200.25)	82 (30, 224.5)	0.898
preAST, Median (Q1,Q3)	51.5 (26.75, 128.75)	60 (26.5, 140.5)	0.957
preCa, Mean ± SD	2.28 ± 0.13	2.27 ± 0.1	0.597
blood_glucose, Median (Q1,Q3)	6.5 (5.7, 7.92)	7 (5.45, 8)	0.393
fibrinogen, Median (Q1,Q3)	3.86 (3.22, 4.87)	3.7 (3.12, 4.23)	0.077
jaundice, n (%)			0.761
0	50 (43)	24 (47)	
1	66 (57)	27 (53)	
tumor_diameter, Median (Q1,Q3)	25 (18, 31)	29 (20.5, 34)	0.133
LN_metastases, n (%)			0.263
0	82 (71)	41 (80)	
1	34 (29)	10 (20)	

Using PyRadiomics (version 3.0.1), 851 radiomic features were extracted from the raw and derived images (Fig. 1b). The dataset comprises 851 radiomic features, including first-order statistics quantifying the voxel intensity distribution within the ROI; shape features describing geometric properties; texture features reflecting gray-level spatial patterns; and filter-based features derived from wavelet, square, square root, logarithmic, and exponential transformations. Wavelet features apply multiscale decomposition (generating subbands: LLL, LLH, LHL, LHH, HLH, HHL, HLL, and HHH) to capture structural hierarchies; square features enhance high-intensity contrast through gray-level squaring; square root features compress the dynamic range via square transformation to mitigate high-value dominance; logarithmic features reduce the intensity range to amplify low-value details; and exponential features emphasize high-intensity local structures through nonlinear amplification. All features were normalized via Z score transformation.

Feature selection and model construction

First, using the binary categorical variable of the presence or absence of perineural invasion in pathological findings as the predictive outcome, Spearman correlation analysis was performed to conduct preliminary dimensionality reduction on normalized radiomic features. Redundant features with interfeature correlations greater than 0.9 redundant features (Spearman correlation > 0.9) were removed, followed by recursive feature elimination (RFE) to retain the top 30 features. LASSO regression with 10-fold cross-validation was applied for final dimensionality reduction. Seven machine learning models—SVM, logistic regression (LR), KNN, decision tree (DT), random forest (RF), Gaussian naive Bayes (GNB), and XGBoost—were trained to predict PNI risk.

Model integration and validation

Clinical predictors (e.g., tumor size, CA19-9, glucose, and lymph node status) were identified via univariate/multivariate logistic regression. A combined radiomic-clinical nomogram was developed. Model performance was evaluated using ROC curves, calibration plots, and decision curve analysis (DCA). Delong's test compared AUC differences between models. The contribution patterns of the five features in the integrated model were conclusively visualized through SHAP-based interpretability analysis.

Statistical analysis

The data were analyzed using Python (version 3.6) and R (version 4.3.2). Continuous variables are expressed as the mean ± SD (normal distribution, Student's t test) or median [IQR] (nonnormal distribution, Mann‒Whitney U test). Categorical variables are reported as frequencies (χ^2 test). Statistical significance was defined as $P < 0.05$.

Table 2 Intergroup differences between perineural invasion and non-perineural invasion groups in training and test cohorts

Characteristics	Training cohort (n = 116)				Validation cohort (n = 51)			
	Total (n = 116)	PNI-negative group (n = 69)	PNI-positive group (n = 47)	p	Total (n = 51)	PNI-negative group (n = 30)	PNI-positive group (n = 21)	p
age, Mean ± SD	62.24 ± 9.25	61.48 ± 9.6	63.36 ± 8.67	0.274	60.94 ± 11.02	59.57 ± 11.76	62.9 ± 9.81	0.276
sex, n (%)				0.497				0.932
female	40 (34)	26 (38)	14 (30)		21 (41)	13 (43)	8 (38)	
male	76 (66)	43 (62)	33 (70)		30 (59)	17 (57)	13 (62)	
high, Median (Q1,Q3)	162 (157, 168)	162 (157, 168)	162 (156.5, 167)	0.66	165 (157.5, 168.5)	165 (160.25, 168)	164 (155, 170)	0.848
weight, Mean ± SD	58.69 ± 8.75	59.13 ± 8.51	58.03 ± 9.14	0.515	60 (50.55, 70.25)	56 (50.83, 63.5)	61.5 (51, 75)	0.231
bmi, Mean ± SD	22.38 ± 2.99	22.49 ± 2.88	22.23 ± 3.16	0.655	22.1 (20.4, 24)	21.95 (19.82, 22.9)	23.4 (20.8, 25.7)	0.083
sughistory, n (%)				0.516				0.505
0	84 (72)	52 (75)	32 (68)		35 (69)	19 (63)	16 (76)	
1	32 (28)	17 (25)	15 (32)		16 (31)	11 (37)	5 (24)	
othercancer, n (%)				0.162				0.293
0	114 (98)	69 (100)	45 (96)		47 (92)	29 (97)	18 (86)	
1	2 (2)	0 (0)	2 (4)		4 (8)	1 (3)	3 (14)	
hbp, n (%)				0.988				0.007
0	90 (78)	53 (77)	37 (79)		38 (75)	27 (90)	11 (52)	
1	26 (22)	16 (23)	10 (21)		13 (25)	3 (10)	10 (48)	
dm, n (%)				1				1
0	90 (78)	54 (78)	36 (77)		35 (69)	21 (70)	14 (67)	
1	26 (22)	15 (22)	11 (23)		16 (31)	9 (30)	7 (33)	
heartdisease, n (%)				1				1
0	109 (94)	65 (94)	44 (94)		48 (94)	28 (93)	20 (95)	
1	7 (6)	4 (6)	3 (6)		3 (6)	2 (7)	1 (5)	
lungdisease, n (%)				1				1
0	110 (95)	65 (94)	45 (96)		50 (98)	29 (97)	21 (100)	
1	6 (5)	4 (6)	2 (4)		1 (2)	1 (3)	0 (0)	
pancreatitishistory, n (%)				0.47				0.412
0	108 (93)	63 (91)	45 (96)		50 (98)	30 (100)	20 (95)	
1	8 (7)	6 (9)	2 (4)		1 (2)	0 (0)	1 (5)	
drink, n (%)				0.709				0.327
0	88 (76)	51 (74)	37 (79)		40 (78)	25 (83)	15 (71)	
1	28 (24)	18 (26)	10 (21)		11 (22)	5 (17)	6 (29)	
smoke, n (%)				0.445				0.957
0	78 (67)	44 (64)	34 (72)		35 (69)	20 (67)	15 (71)	
1	38 (33)	25 (36)	13 (28)		16 (31)	10 (33)	6 (29)	
NAHA, n (%)				0.541				0.481
I	6 (5)	5 (7)	1 (2)		2 (4)	2 (7)	0 (0)	
II	63 (54)	36 (52)	27 (57)		23 (45)	12 (40)	11 (52)	

Table 2 (continued)

Characteristics	Training cohort (n = 116)				Validation cohort (n = 51)			
	Total (n = 116)	PNI-negative group (n = 69)	PNI-positive group (n = 47)	p	Total (n = 51)	PNI-negative group (n = 30)	PNI-positive group (n = 21)	p
III	47 (41)	28 (41)	19 (40)		26 (51)	16 (53)	10 (48)	
ASA, n (%)				0.764				0.572
I	14 (12)	9 (13)	5 (11)		7 (14)	3 (10)	4 (19)	
II	80 (69)	49 (71)	31 (66)		38 (75)	24 (80)	14 (67)	
III	20 (17)	10 (14)	10 (21)		6 (12)	3 (10)	3 (14)	
IV	2 (2)	1 (1)	1 (2)		0	0	0	
NLR, Median (Q1,Q3)	3.18 (2.34, 4.19)	3.29 (2.26, 4.43)	3.11 (2.44, 3.74)	0.545	2.98 (2.2, 4.06)	2.93 (2.21, 3.86)	3.41 (2.23, 6.19)	0.476
PLR, Median (Q1,Q3)	185.76 (141.16, 244.79)	187.83 (140.65, 260.95)	182.58 (144.84, 231.77)	0.487	176.58 (135.8, 232.55)	164.4 (115.89, 223.81)	183.48 (159.56, 279.03)	0.073
LMR, Median (Q1,Q3)	3.18 (2.34, 4.19)	3.29 (2.26, 4.43)	3.11 (2.44, 3.74)	0.545	2.98 (2.2, 4.06)	2.93 (2.21, 3.86)	3.41 (2.23, 6.19)	0.476
prognostic_nutritional_index, Mean ± SD	46.16 ± 5.71	46.19 ± 5.74	46.11 ± 5.73	0.943	45.35 ± 6.36	44.96 ± 7.1	45.91 ± 5.24	0.584
SII, Median (Q1,Q3)	708.12 (452.08, 1082.32)	714 (448.34, 1219.16)	697.37 (483.6, 934.17)	0.5	586.29 (430.9, 1010.71)	535.17 (387.34, 740.65)	841.34 (529.74, 1043.4)	0.059
preWBC, Median (Q1,Q3)	5.64 (4.65, 7.2)	5.87 (4.8, 7.56)	5.57 (4.46, 6.89)	0.475	5.76 (4.86, 6.72)	5.19 (4.57, 6.64)	6.15 (5.31, 6.77)	0.32
prePLT, Mean ± SD	228.8 ± 73	232.52 ± 72.1	223.34 ± 74.73	0.512	215.67 ± 68.95	196.7 ± 47.23	242.76 ± 85.67	0.033
preNC, Median (Q1,Q3)	3.76 (2.99, 5.15)	3.93 (2.89, 5.35)	3.69 (3, 4.88)	0.566	3.65 (2.96, 4.8)	3.4 (2.86, 4.77)	4.08 (3.34, 4.81)	0.243
preLC, Median (Q1,Q3)	1.12 (0.94, 1.51)	1.12 (0.95, 1.5)	1.13 (0.94, 1.51)	0.893	1.27 (0.92, 1.46)	1.21 (0.9, 1.46)	1.28 (1.02, 1.44)	0.992
preMC, Median (Q1,Q3)	0.48 (0.36, 0.62)	0.47 (0.36, 0.63)	0.48 (0.38, 0.6)	0.853	0.42 (0.37, 0.54)	0.39 (0.35, 0.5)	0.46 (0.4, 0.58)	0.094
CA199, Median (Q1,Q3)	237.5 (78.22, 554.55)	124.8 (22.2, 493.1)	427.65 (201.38, 632.75)	<0.001	191.7 (54.45, 399.25)	76 (22.92, 240.85)	249.8 (127.8, 481.1)	0.015
CEA, Median (Q1,Q3)	3.75 (2.38, 5.6)	3.7 (2.3, 5.3)	3.8 (2.6, 5.7)	0.702	3.1 (1.94, 4.35)	3.15 (1.8, 5.12)	3.1 (2.2, 4)	0.947
preHb, Mean ± SD	124.74 ± 17.55	125.45 ± 17.92	123.7 ± 17.15	0.598	122.86 ± 17.2	122.5 ± 16.84	123.38 ± 18.1	0.861
preAlb, Mean ± SD	39.92 ± 4.89	40.01 ± 4.71	39.79 ± 5.17	0.81	38.92 ± 4.96	38.3 ± 5.44	39.81 ± 4.15	0.267
preTB, Median (Q1,Q3)	72.95 (11.9, 146.3)	67.2 (11.7, 127.9)	83.4 (13.75, 168.35)	0.559	69.8 (13.5, 151.1)	50.9 (9.95, 130.43)	102.6 (26.6, 153.6)	0.174
preALT, Median (Q1,Q3)	70.5 (25, 200.25)	60 (22, 159)	79 (25.5, 252.5)	0.172	82 (30, 224.5)	61 (25.5, 148.75)	175 (55, 279)	0.114
preAST, Median (Q1,Q3)	51.5 (26.75, 128.75)	45 (25, 112)	63 (29, 177.5)	0.109	60 (26.5, 140.5)	35 (23.75, 111.75)	80 (42, 171)	0.123
preCa, Mean ± SD	2.28 ± 0.13	2.28 ± 0.12	2.29 ± 0.14	0.666	2.27 ± 0.1	2.27 ± 0.1	2.28 ± 0.11	0.64
blood_glucose, Median (Q1,Q3)	6.5 (5.7, 7.92)	5.9 (5.3, 6.8)	6.8 (6.55, 9.3)	<0.001	7 (5.45, 8)	6.65 (5.32, 7.68)	7.9 (6.8, 10.8)	0.028
fibrinogen, Median (Q1,Q3)	3.86 (3.22, 4.87)	3.83 (3.08, 4.79)	3.95 (3.4, 4.93)	0.412	3.7 (3.06, 4.07)	3.33 (2.97, 3.96)	3.96 (3.54, 4.25)	0.037
jaundice, n (%)				0.502				0.827
0	50 (43)	32 (46)	18 (38)		24 (47)	15 (50)	9 (43)	
1	66 (57)	37 (54)	29 (62)		27 (53)	15 (50)	12 (57)	
tumor_diameter, Median (Q1,Q3)	25 (18, 31)	27 (21, 34)	21 (15.5, 27.5)	0.001	29 (20.5, 34)	32 (23.5, 38.25)	24 (19, 29)	0.007
LN_metastases, n (%)				0.005				0.015
0	82 (71)	56 (81)	26 (55)		33 (65)	24 (80)	9 (43)	
1	34 (29)	13 (19)	21 (45)		18 (35)	6 (20)	12 (57)	

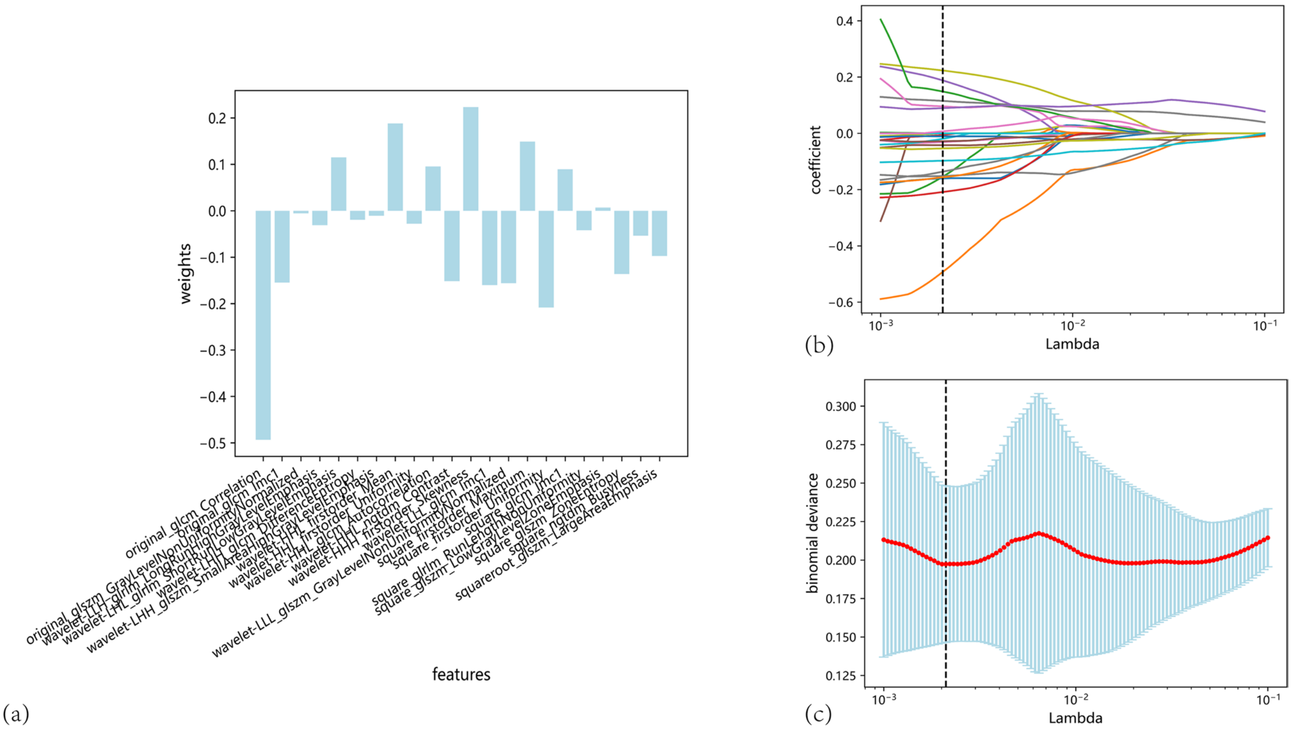

Fig. 3 **a** Twenty-two radiomic features were selected through LASSO regression. **b** Coefficient variation curves of features selected by LASSO regression, where the black dashed line indicates the optimal lambda value. Each curve represents the trajectory of coefficient variation for individual features. **c** Binomial deviance versus lambda plot for Lasso feature selection. The black dashed line denotes the optimal lambda value (0.002) determined through 10-fold cross-validation in LASSO regression

The R packages twogroups, glm, pROC, and ggplot2 were used for baseline analysis, logistic regression, and visualization.

Results

Cohort baseline characteristics

A total of 182 patients who underwent radical pancreatic resection with pathologically confirmed pancreatic ductal adenocarcinoma (PDAC) at the First Affiliated Hospital of Chongqing Medical University between January 2018 and December 2024 were initially enrolled. After applying the inclusion and exclusion criteria, 167 patients were included in the analysis (Fig. 2). The cohort comprised 106 males and 61 females aged 31–82 years. Using a random seed of 38, the dataset was divided into a training cohort (116 cases) and a test cohort (51 cases), with no significant differences in baseline clinical characteristics between the two groups (Table 1).

In the training cohort, 47 patients exhibited pathologically confirmed perineural invasion (PNI-positive), while 69 were PNI-negative. Compared with the PNI-positive group, the PNI-negative group had significantly larger maximum tumor diameters ($P < 0.05$). Conversely, the PNI-positive group presented higher CA19-9 levels, blood glucose concentrations, and lymph node metastasis rates ($P < 0.05$). In the internal validation cohort (51 patients), 21 were PNI-positive, and 30 were PNI-negative. Similar to the training cohort, the PNI-negative group had larger tumor diameters, whereas the PNI-positive group presented elevated fibrinogen levels, CA19-9 levels, blood glucose levels, lymph node metastasis rates, and preoperative platelet counts ($P < 0.05$) (Table 2).

Radiomic feature selection and model construction

Of the extracted 851 radiomic features, 318 nonredundant features (Spearman correlation coefficient < 0.9) were retained. Recursive feature elimination (RFE) identified the top 30 features, and LASSO regression Further narrowed these to 22 key features (Fig. 3a). The optimal LASSO regularization parameter (λ) was 0.002 (Fig. 3c), with feature coefficients ranging from − 0.6 to 0.4 (Fig. 3b). These 22 features were used to train seven machine learning models.

The Gaussian naive Bayes (GNB) model demonstrated superior performance, with AUC values of 0.899 (training cohort) and 0.813 (validation cohort) (Fig. 4a, b). The corresponding accuracy, sensitivity, and specificity were 0.801/0.725, 0.957/0.762, and

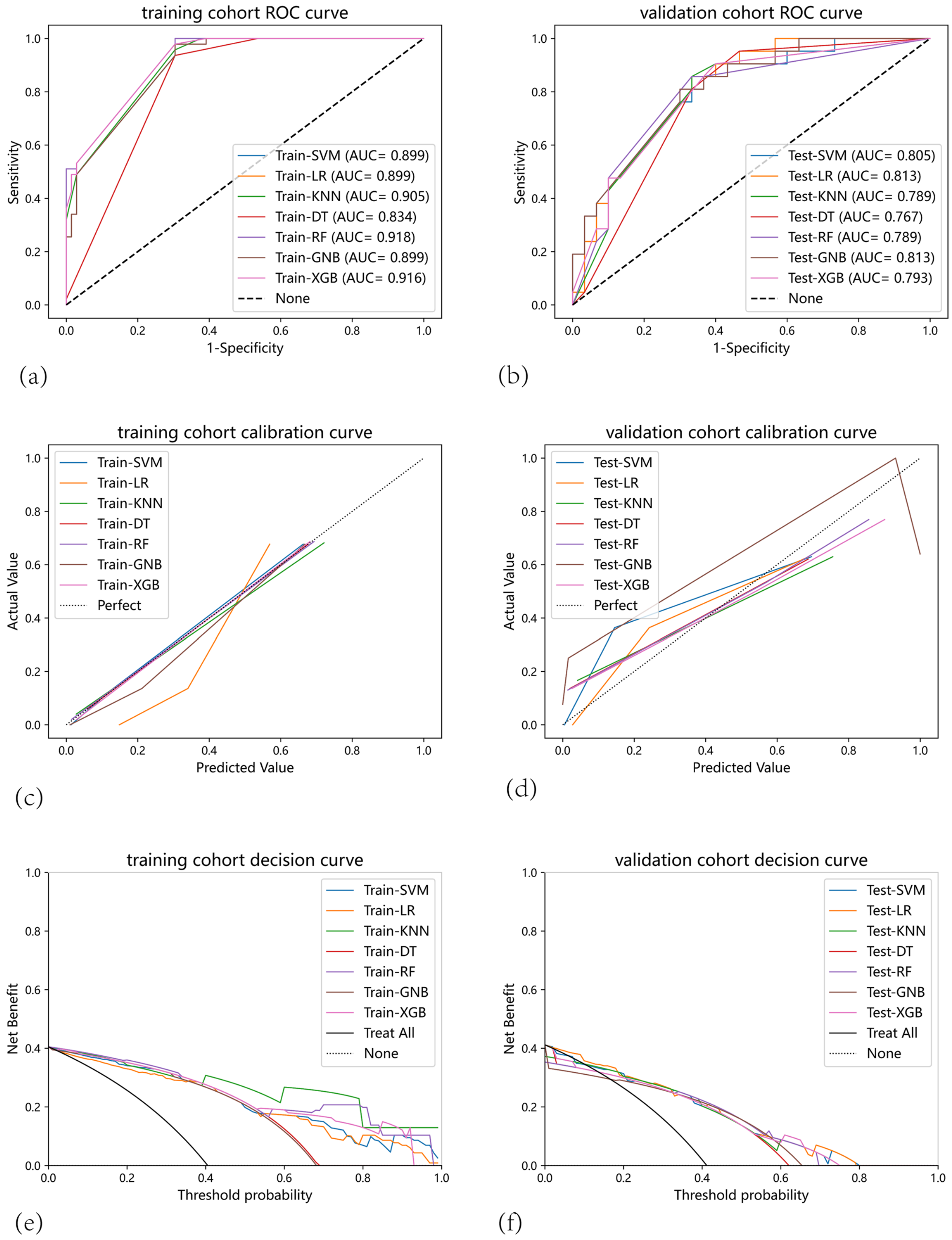

Fig. 4 (See legend on next page.)

(See figure on previous page.)

Fig. 4 Performance evaluation of seven machine learning algorithms for predicting perineural invasion. **a** Receiver operating characteristic (ROC) curves demonstrated the predictive efficacy of different machine learning algorithms for perineural invasion in the training cohort. (SVM-AUC: 0.899, LR-AUC: 0.899, KNN-AUC: 0.905, DT-AUC: 0.834, RF-AUC: 0.918, GNB-AUC: 0.899, XGB-AUC: 0.916) (**b**) ROC curves illustrate the performance of these algorithms in the validation cohort. (SVM-AUC:0.805, LR-AUC:0.813, KNN-AUC:0.789, DT-AUC:0.767, RF-AUC:0.789, GNB-AUC:0.813, XGB-AUC:0.793) (**c**, **d**) Calibration curves assessed the agreement between the predicted probabilities and observed outcomes across both the training and validation cohorts.(**e**, **f**) Decision curve analysis (DCA) evaluated the clinical utility of the seven machine learning models in predicting perineural invasion within the training (threshold:0.6–1.0) and validation (threshold:0.6–0.8) cohorts

0.696/0.700, respectively (Table 3). The calibration curves closely aligned with the ideal diagonal (Fig. 4c, d), indicating strong agreement between the predicted and observed PNI probabilities. Decision curve analysis (DCA) revealed optimal clinical utility at a risk threshold of 0.6–0.8, where the GNB model provided the highest net benefit (Fig. 4e, f).

Clinical risk factors for perineural invasion

Univariate logistic regression revealed that the maximum tumor diameter, lymph node metastasis rate, CA19-9 level, and blood glucose concentration were significant risk factors for PNI. Multivariate analysis confirmed these factors as independent predictors (Table 4).

Predictive performance of the integrated models

The combined radiomic-clinical model outperformed the standalone models. In the training cohort, the AUC values were 0.945 (combined), 0.899 (radiomics), and 0.758 (clinical) (Fig. 5a, b). The validation cohort yielded AUCs of 0.881, 0.813, and 0.729, respectively (Table 5). Delong's test confirmed that the AUC of the combined model was significantly greater than that of both the clinical and radiomics models ($P < 0.05$) (Table 6). A nomogram integrating radiomic and clinical features was developed (Fig. 5e), with calibration curves demonstrating high concordance between the predicted and actual PNI probabilities (Fig. 5f). DCA revealed a superior net benefit for the radiomics and combined models at thresholds of 0.8–1.0 (Fig. 5c, d). Fivefold cross-validation reinforced the stability of the combined model (Table 7), with mean AUCs of 0.905 (training) and 0.882 (validation) (Fig. 6a, b).

SHAP Visualization of the integrated model

Our study employed the SHAP interpretability framework to elucidate the predictive mechanism of the Gaussian naive Bayes (GNB) model for perineural invasion (PNI). Global feature analysis revealed that the radiomic score (radscore) made the greatest contribution to model decisions, with the top five features collectively dominating the predictive outcomes, achieving a cumulative contribution level of statistical significance (Fig. 7a). Heatmaps were used to visualize the directional effects and magnitudes of each feature through color gradients, where red regions represented positive drivers (e.g., specific imaging texture parameters) and blue regions denoted negative suppressors (e.g., uniformity metrics) (Fig. 7b, c). For individual prediction, SHAP waterfall plots quantified feature contributions at the case level: the baseline probability reflected the model's initial predictive value, whereas SHAP values modulated the final probability f(x) through directional (positive/negative) and amplitude adjustments, which were calculated as the linear superposition of baseline values and feature contributions (Fig. 8). SHAP dependence plots further revealed nonlinear interaction patterns of key features. As feature values vary along the x-axis, fluctuations in SHAP values on the y-axis directly reflect the variable's threshold effects on PNI risk, with SHAP values > 0 indicating a model inclination toward positive predictions (Fig. 9). This methodology systematically clarifies the logical chain from global decision patterns to individualized predictions in GNB models, establishing a standardized framework for the biological interpretation of integrated medical imaging models.

To Further explore the clinical significance of specific radiomic features, we visualized the 22 individual features

Table 3 AUC, Accuracy, Sensitivity, and Specificity of Radiomics Models Based on Seven Machine Learning Algorithms in Training and Test Cohorts

Model Types	Training cohort				Validation cohort			
	AUC	Accuracy	Sensitivity	Specificity	AUC	Accuracy	Sensitivity	Specificity
SVM	0.898705	0.801724	0.957	0.696	0.804762	0.705882	0.762	0.667
LR	0.898705	0.775862	0.489	0.971	0.812698	0.705882	0.429	0.9
KNN	0.905026	0.801724	0.957	0.696	0.788889	0.72549	0.81	0.667
DT	0.83395	0.793103	0.936	0.696	0.72549	0.76746	0.81	0.667
RF	0.91844	0.810345	0.979	0.696	0.788889	0.745098	0.857	0.667
GNB	0.898705	0.801724	0.957	0.696	0.812698	0.72549	0.762	0.7
XGB	0.91551	0.810345	0.979	0.696	0.792857	0.72549	0.857	0.633

Table 4 Univariate and multivariate analyses of clinical characteristics associated with perineural invasion

Characteristics	OR	OR.95L	OR.95H	*p*value
	Univariate analysis			
age	1.022794	0.981685	1.065625	0.281556
sex	1.425249	0.645298	3.147904	0.380774
high	0.98712	0.935576	1.041504	0.635654
weight	0.985526	0.944104	1.028764	0.505712
bmi	0.970995	0.856583	1.100688	0.645404
sughistory	1.433824	0.630124	3.262611	0.390336
othercancer	8828646	0	Inf	0.987601
hbp	0.89527	0.365913	2.190434	0.808516
dm	1.1	0.454001	2.665194	0.83282
heartdisease	1.107955	0.236322	5.194448	0.896532
lungdisease	0.722222	0.126839	4.112334	0.713854
pancreatitishistory	0.466667	0.090037	2.418749	0.363958
drink	0.765766	0.317211	1.848603	0.552834
smoke	0.672941	0.300599	1.506493	0.335378
NAHA	3.75	0.413748	33.98807	0.239887
ASA	1.138776	0.349176	3.71391	0.829407
NLR	0.953754	0.858567	1.059493	0.377418
PLR	0.998244	0.99481	1.001691	0.317652
LMR	0.953754	0.858567	1.059493	0.377418
prognostic_nutritional_index	0.997598	0.934654	1.064781	0.94234
SII	0.999811	0.999397	1.000225	0.370888
preWBC	0.941335	0.786474	1.126689	0.509742
prePLT	0.998241	0.993083	1.003425	0.505226
preNC	0.91764	0.746373	1.128207	0.414804
preLC	1.130118	0.534573	2.389132	0.748774
preMC	1.080746	0.164157	7.11523	0.935635
CA199	1.001439	1.000423	1.002456	0.005495
CEA	0.975092	0.892943	1.0648	0.574309
preHb	0.994296	0.973402	1.015639	0.597588
preAlb	0.990427	0.917631	1.068997	0.804931
preTB	1.001075	0.996605	1.005565	0.637981
preALT	1.001585	0.999123	1.004053	0.207237
preAST	1.002263	0.998873	1.005664	0.191076
preCa	1.967741	0.102044	37.94444	0.653925
blood_glucose	1.214594	1.044514	1.412368	0.011544
fibrinogen	1.084074	0.802552	1.46435	0.598747
jaundice	1.393393	0.65503	2.964054	0.389015
tumor_diameter	0.944977	0.906815	0.984745	0.007126
LN_metastases	3.47929	1.511799	8.007322	0.00337
	Multivariate analysis			
CA199	1.001244	1.000058	1.002432	0.039866
blood_glucose	1.173121	1.001135	1.374651	0.048382
tumor_diameter	0.925399	0.87985	0.973305	0.002607
LN_metastases1	3.887643	1.502817	10.05696	0.005111

composing the Radscore using SHAP analysis. The results demonstrated that wavelet_HHL_glcm_Autocorrelation, square_ngtdm_Busyness, square_glrlm_RunLengthNonUniformity, and squareroot_glszm_LargeAreaEmphasis contributed substantially to PNI prediction and correlated with PNI positivity rates (Fig. 10a, b). Wavelet-HHL_glcm_Autocorrelation represents the autocorrelation feature value calculated via the gray-level

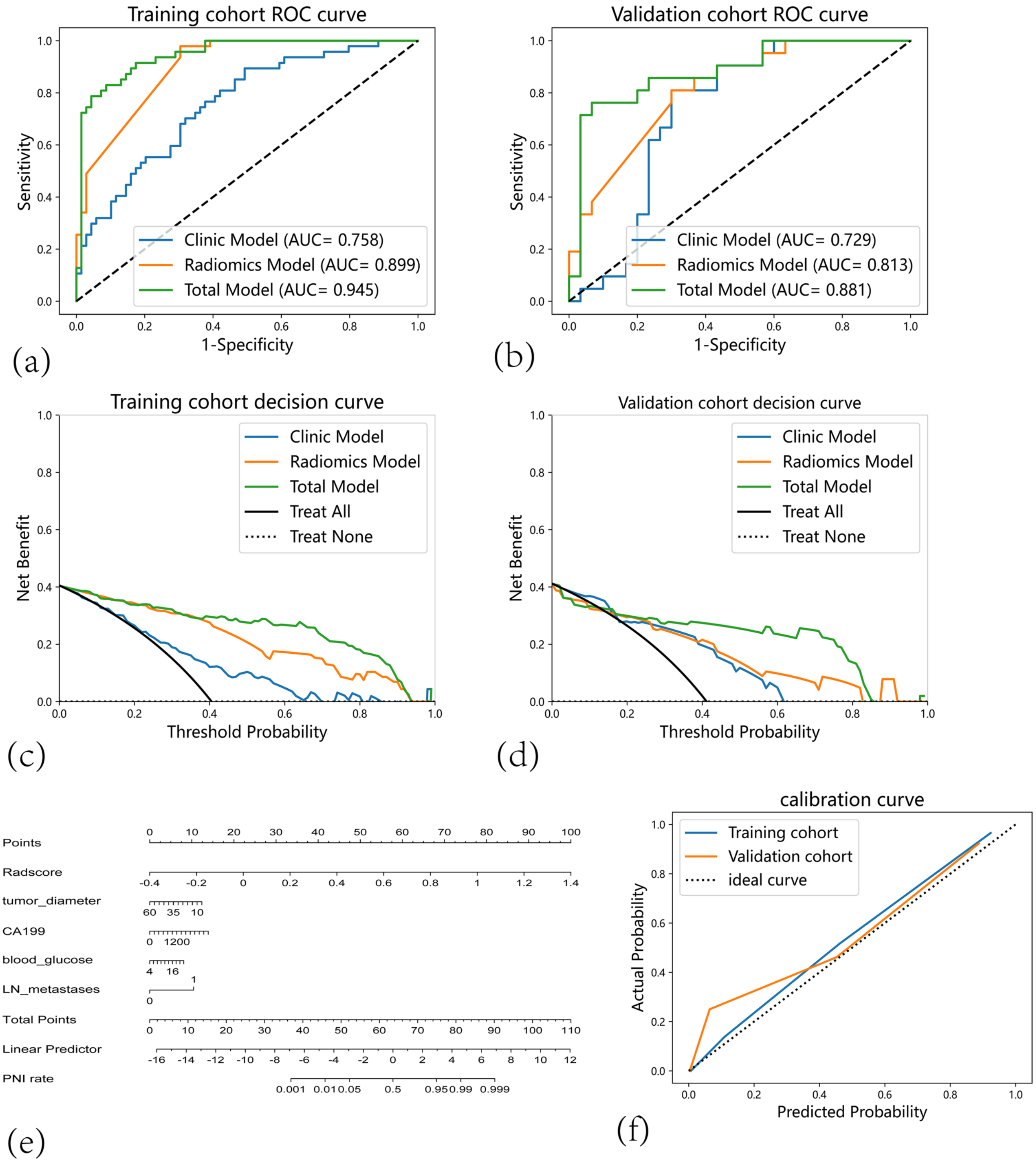

Fig. 5 **a** ROC curves demonstrate the predictive efficacy of the three models for perineural invasion in the training cohort. **b** ROC curves illustrate the performance of the three models in the validation cohort. The x-axis represents specificity, and the y-axis represents sensitivity. **c**, **d** Decision curve analysis (DCA) evaluates the clinical utility of the three models in predicting perineural invasion within the training and validation cohorts. The x-axis represents the threshold probability, and the y-axis represents the net benefit. **e** A nomogram was constructed on the basis of CECT features and clinical characteristics associated with perineural invasion. **f** Calibration curves of the total models in the training cohort and validation cohorts. The x-axis represents the predicted probability, and the y-axis represents the actual probability

Table 5 Performance metrics of optimal machine learning algorithm-based models: auc, accuracy, sensitivity, and specificity for radiomics, clinical, and total models

Model	cohort	AUC(95%CI)	accuracy	sensitivity	specificity
Clinic Model	Training cohort	0.758 [0.668, 0.842]	0.698	0.553	0.797
	Validation cohort	0.729[0.579, 0.870]	0.706	0.667	0.733
Radiomics Model	Training cohort	0.899[0.846, 0.942]	0.802	0.957	0.696
	Validation cohort	0.813[0.682, 0.916]	0.725	0.762	0.7
Total Model	Training cohort	0.945 [0.899, 0.981]	0.871	0.787	0.928
	Validation cohort	0.881[0.764, 0.971]	0.843	0.762	0.9

Table 6 DeLong test for comparing statistics among the three models

Comparison	Training cohort		Validation cohort	
	statistics	*p*	statistics	*p*
Clinic Model VS Radiomics Model	-2.632	0.00849	-0.858	0.39076
Radiomics Model VS Total Model	-2.004	0.04503	-1.71173	0.08695
Clinic Model VS Total Model	-4.981	<0.00001	-2.004	0.04504

Table 7 Performance metrics of optimal machine learning algorithm-based models: auc, accuracy, sensitivity, and specificity for 5-fold cross-validation

Model	cohort	AUC (95%CI)	accuracy	sensitivity	specificity
Fold 1	Training cohort	0.91[0.848, 0.957]	0.85	0.732	0.935
	Validation cohort	0.864[0.696, 0.975]	0.824	0.75	0.864
Fold 2	Training cohort	0.882[0.816, 0.941]	0.842	0.75	0.909
	Validation cohort	0.939[0.839, 0.996]	0.853	0.667	0.955
Fold 3	Training cohort	0.904[0.848, 0.955]	0.821	0.679	0.914
	Validation cohort	0.889[0.754, 0.981]	0.758	0.667	0.833
Fold 4	Training cohort	0.912[0.854, 0.959]	0.828	0.717	0.901
	Validation cohort	0.881[0.719, 1.000]	0.758	0.607	1
Fold 5	Training cohort	0.92[0.868, 0.960]	0.843	0.722	0.925
	Validation cohort	0.835[0.670, 0.954]	0.848	0.786	0.895

co-occurrence matrix (GLCM) in the HHL wavelet-decomposed image subband. It captures texture repetitiveness along the horizontal direction, highlighting the transverse heterogeneity and tissue structural regularity of lesions. This feature is closely associated with invasive growth boundaries in PNI. Square_ngtdm_Busyness quantifies the intensity of local gray-level variations using the neighborhood gray-tone difference matrix (NGTDM) after square filter preprocessing, reflecting microscopic heterogeneity in lesion regions. Infiltrative PNI growth may disrupt native tissue texture, inducing localized gray-level fluctuations. Square_glrlm_RunLengthNonUniformity is a key feature characterizing the spatial nonuniformity of texture distribution through the gray-level run-length matrix (GLRLM). It quantifies microstructural heterogeneity within lesions and serves as a critical metric for evaluating high-risk pathological characteristics such as pancreatic neuroinvasion. Squareroot_glszm_LargeAreaEmphasis measures the spatial distribution of large contiguous areas in lesions using the gray-level size zone matrix (GLSZM) with square-root filter preprocessing, which reflects pathological properties such as necrosis or fibrosis within tumors. Its relevance may stem from the neuronal necrosis induced by PNI.

Discussion

Pancreatic cancer is one of the most aggressive solid malignancies, and its poor prognosis is attributed to multiple factors, including malignant biological behavior, late diagnosis, early recurrence/metastasis, and therapeutic resistance [24]. Notably, perineural invasion (PNI) is closely associated with tumor progression, increased local recurrence, severe pain, and unfavorable outcomes in patients with pancreatic cancer [7]. Consequently, there is an urgent need for effective preoperative clinical and imaging-based predictors of PNI probability to guide prognosis assessment, adjuvant therapy planning, and intraoperative decision-making. Previous studies have highlighted the potential of radiomics in predicting lymph node metastasis, recurrence, and occult metastasis in patients with pancreatic cancer [25–27], yet few

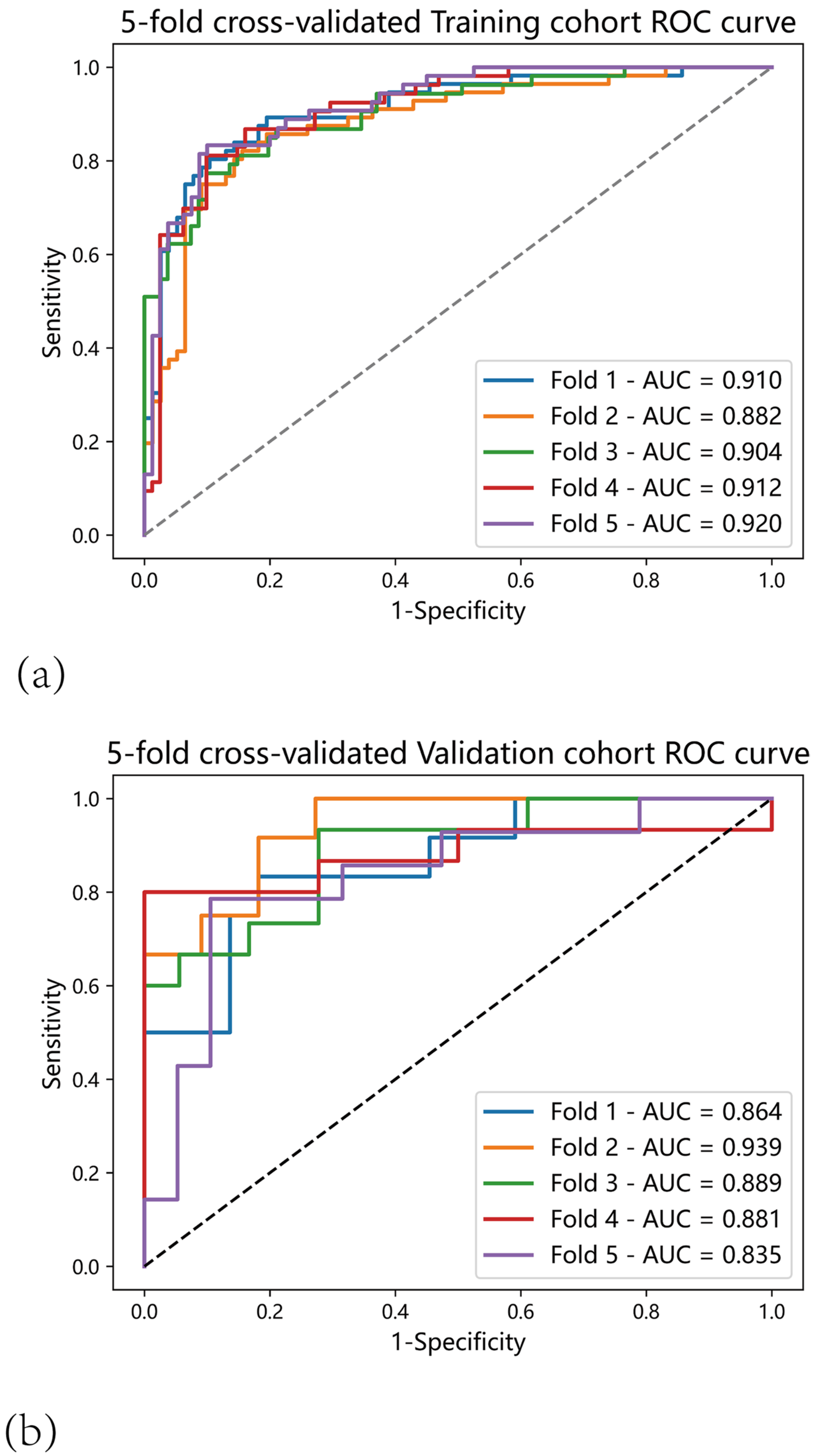

Fig. 6 ROC curves of the total model with 5-fold cross-validation across the training (**a**) and validation (**b**) cohorts. The x-axis represents specificity, and the y-axis represents sensitivity

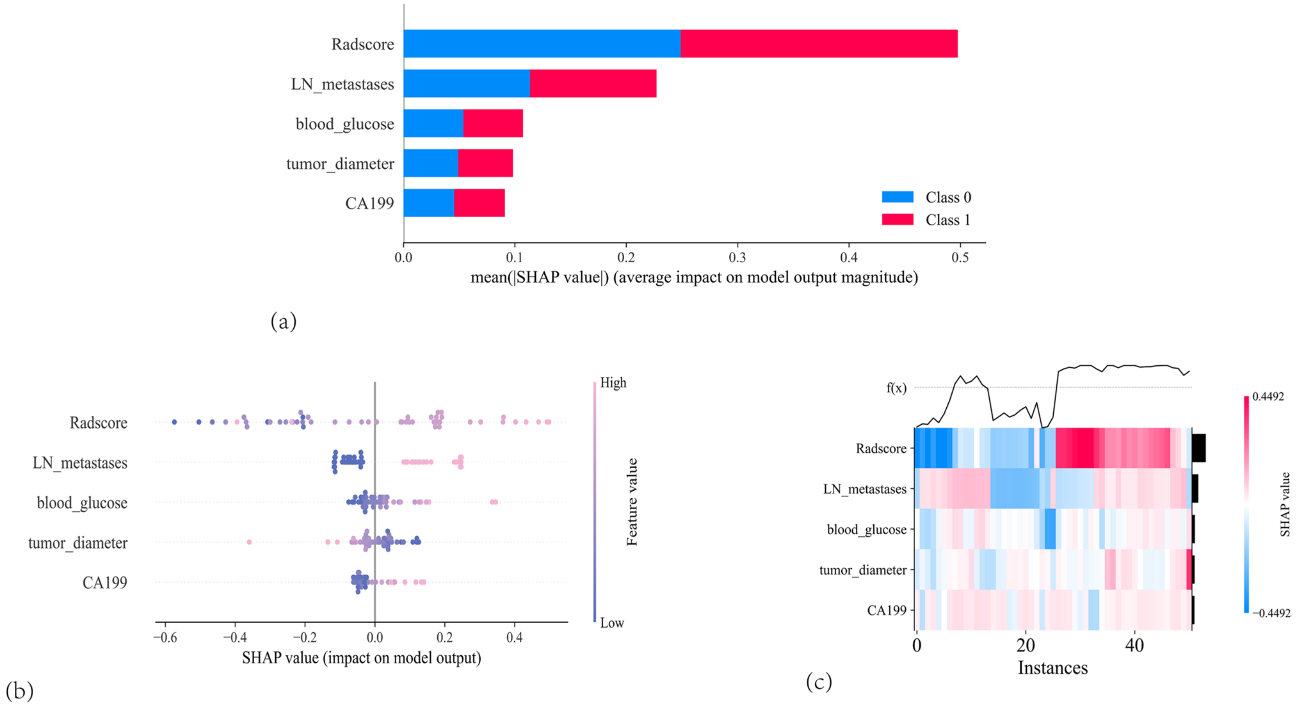

(a)

(b)

(c)

Fig. 7 **a** SHAP bar summary plot of the five features in the integrated model. **b** SHAP dot summary plot of the five features in the integrated model. **c** SHAP heatmap of the five features in the integrated model. The x-axis represents the SHAP values that describe the impact of each feature on model prediction. Positive SHAP values indicate an increased risk of PNI, whereas negative SHAP values indicate a decreased risk

studies have focused on its role in predicting PNI. Importantly, PNI has been shown to outperform the T stage and nodal status in predicting early recurrence after pancreaticoduodenectomy for patients with pancreatic head adenocarcinoma [28], underscoring the prognostic value of radiomics-based PNI prediction.

In this study, we extracted 851 radiomic features from preoperative abdominal CT images and identified 22 key features through Spearman correlation analysis, recursive feature elimination (RFE), and LASSO regression. These features encompass multidimensional information related to the tumor texture, gray-level distribution, contrast, frequency-domain characteristics, shape, statistical properties, boundary features, higher-order statistics, and local heterogeneity. Using these features, we developed a radiomic-clinical integrated model that demonstrated robust performance in predicting PNI, achieving AUC values of 0.899 (training cohort) and 0.813 (validation cohort). While prior studies have linked traditional clinical markers—such as CA19-9, blood glucose, and total serum bilirubin—to PNI risk [19], our radiomics and combined models exhibited superior predictive accuracy compared with clinical feature-only models (AUC: 0.753 training, 0.737 validation [19]).

Interestingly, our model revealed an inverse correlation between tumor size and PNI incidence, aligning with reports that even sub2 cm pancreatic cancers exhibit high PNI rates [29]. This paradox may reflect earlier clinical detection of smaller tumors due to neuropathic pain caused by neural plexus invasion. Additionally, the positive association between lymph node metastasis and PNI underscores the aggressive biology of pancreatic cancer, where invasive and metastatic behaviors are intertwined. CA19-9, a diagnostic marker for pancreatic cancer, has elevated preoperative serum levels in patients with perineural invasion compared with controls. Furthermore, CA19-9 levels progressively increase with increasing pathological grade, suggesting its potential as a biomarker for neural invasion in patients with pancreatic cancer [30]. Hyperglycemia, a recognized risk factor for pancreatic cancer, may promote neural infiltration through glucose neurotoxicity mechanisms involving polyol pathway activation, glucose-driven oxidative stress, and protein glycosylation. Experimental evidence from Capan-1 pancreatic ductal adenocarcinoma cells has demonstrated that hyperglycemia specifically activates the polyol pathway by increasing aldose reductase expression and activity [31]– [32]. These findings support the hypothesis that chronic hyperglycemia induces pancreatic oxidative stress, subsequently activating the protein kinase C and NF-κB pathways to facilitate neural invasion [33]. Furthermore, studies indicate that

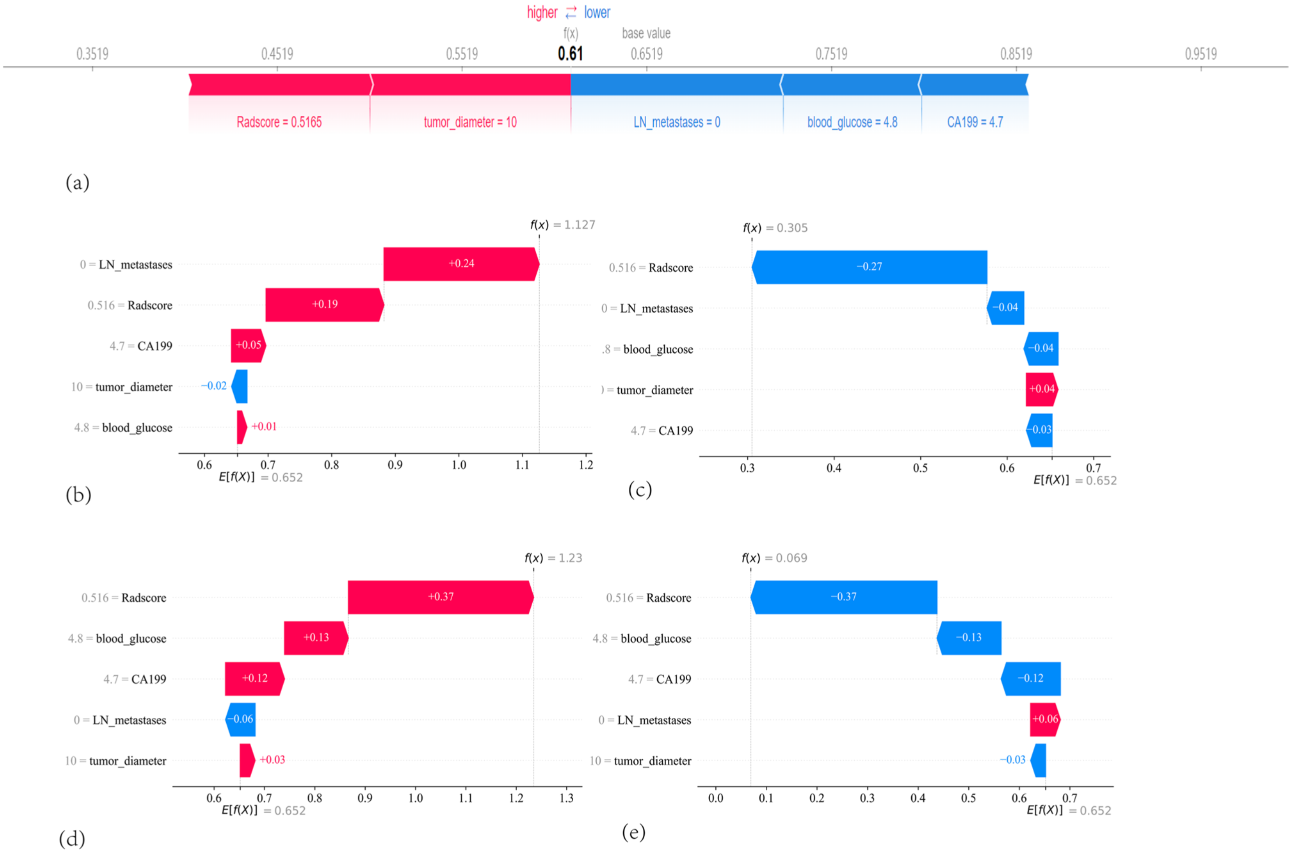

Fig. 8 **a** Case-specific SHAP force plot for one PNI-negative patient. **b**, **d** Case-specific SHAP waterfall plot for two PNI-positive patients. **c**, **e** Case-specific SHAP waterfall plot for two PNI-negative patients. On waterfall plots, the value at the bottom represents the expected value of the model output, and each row represents the contribution of each feature to the model output. The red arrow indicates an increased risk of PNI, whereas the blue arrow indicates a decreased risk. The gray text before the feature names shows the value of each feature for the case

hyperglycemia not only enhances cancer cell proliferation (potentially upregulating nerve growth factors) but also promotes nerve demyelination and axonal degeneration, creating a microenvironment conducive to neural infiltration [34]. These findings collectively corroborate the clinical biomarker correlations with PNI identified in our study.

Advancements in medical imaging have revealed subtle yet prognostically significant tumor features [35]. Although histopathology remains the gold standard for pancreatic cancer diagnosis, its reliance on postoperative specimens limits its utility in nonsurgical candidates (15–20% of patients at diagnosis [36, 37]). For these patients, preoperative radiomics-based PNI prediction could guide therapeutic strategies and surgical candidacy reassessment. Furthermore, radiomic analysis of PNI may enable early identification of aggressive disease and inform neoadjuvant therapy decisions for patients with resectable disease. By converting imaging data into quantitative biomarkers, radiomics not only predicts the biological traits of pancreatic cancer (e.g., PNI, microvascular invasion) but also links tumor microenvironment heterogeneity with molecular pathways. For example, emerging evidence links PNI to exosomal lncRNA XIST-mediated miR-211–5p/GDNF signaling [38] and cholinergic pathway-induced immunosuppression [39]. Integrating radiomics with genomic data could thus uncover novel biomarkers and mechanistic insights into tumor progression.

Despite the limited studies on the use of radiomics for PNI prediction, recent work highlights the potential of imaging. Guo et al. proposed the tumor-artery distance as a diagnostic marker for extrapancreatic PNI (EPNI) and developed a plexus pancreaticus capitalis (PLX)-based classification to guide resection margins [40]. Similarly, 3D volume-rendered MDCT has improved EPNI detection, which is correlated with poorer survival post-pancreaticoduodenectomy [41]– [42]. However, subjective variability in CT-based PNI assessment is a challenge [16]. Our model mitigates this by combining radiomic

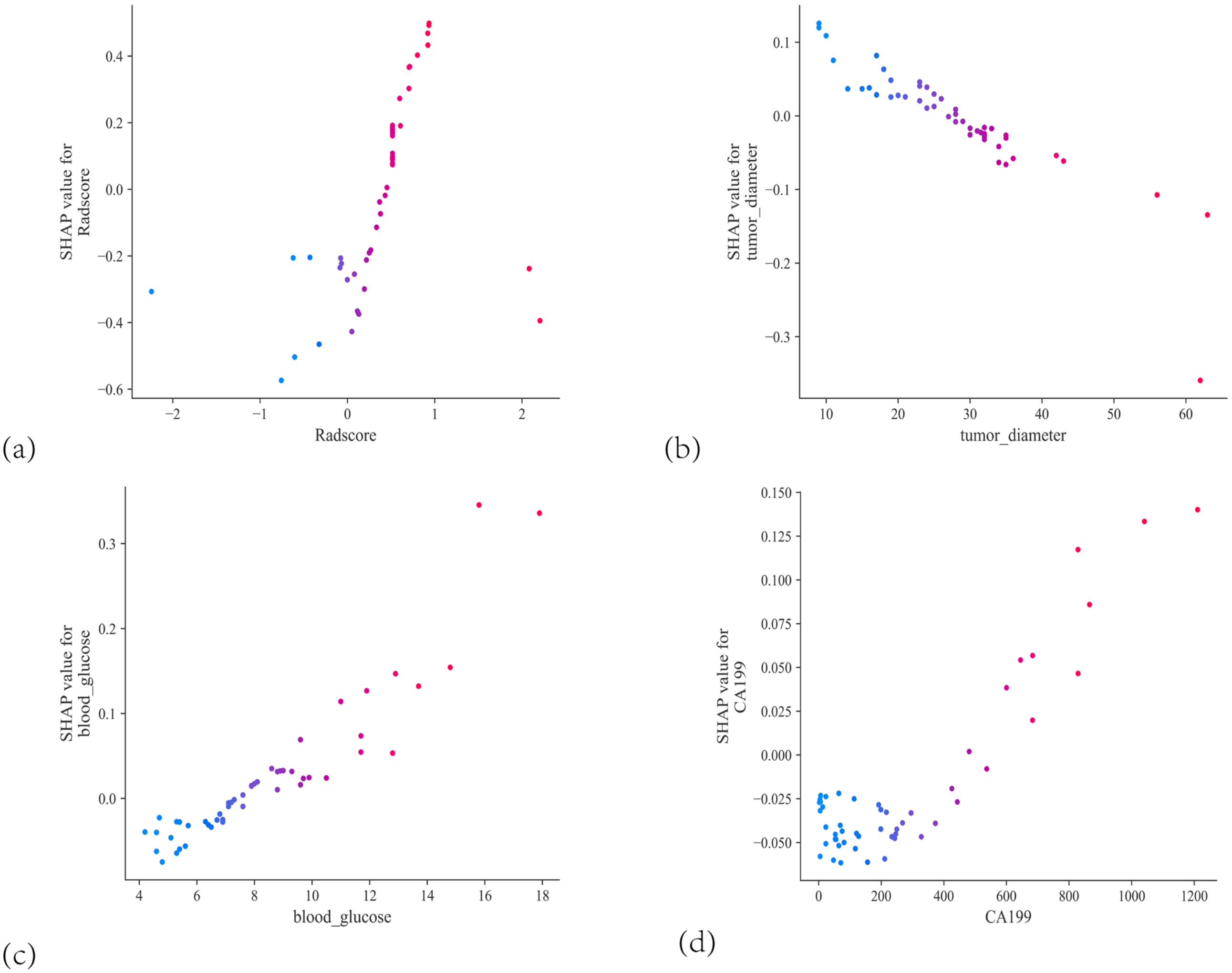

Fig. 9 **a** SHAP dependence plot for the Radscore feature (**b**) SHAP dependence plot for the tumor diameter feature. **c** SHAP dependence plot for blood glucose features. **d** SHAP dependence plot for the CA-199 feature. Each dependence plot shows how a single feature affects the output of the prediction model, and each dot represents a single patient

and clinical features, which enhances both objectivity and accuracy.

Limitations and future directions

This study has several limitations. The most significant limitations of this study stem from its single-center retrospective design and absence of external validation. Relying solely on data from a single institution with an internal validation cohort that share the same origin as the training set (identical institution/time frame) introduces the risk of selection bias and severely constrains the generalizability of the ML conclusions. The lack of authentic external validation (using data from diverse centers, scanner models, and patient populations) significantly compromises the robustness and clinical applicability of the radiomic model, a concern further accentuated by the observed higher AUC in the validation cohort than in the training cohort (potentially indicating overfitting owing to limited sample size). Furthermore, despite standardized protocols, technical heterogeneity in CT scanners and imaging parameters across institutions may affect feature reproducibility. Therefore, the foremost future priority is to conduct multicenter prospective external validation (requiring cross-institutional imaging protocol standardization or data normalization techniques to resolve technical heterogeneity) while concurrently exploring interaction mechanisms between radiomic features and molecular biomarkers (e.g., KRAS mutations) to deepen biological interpretation.

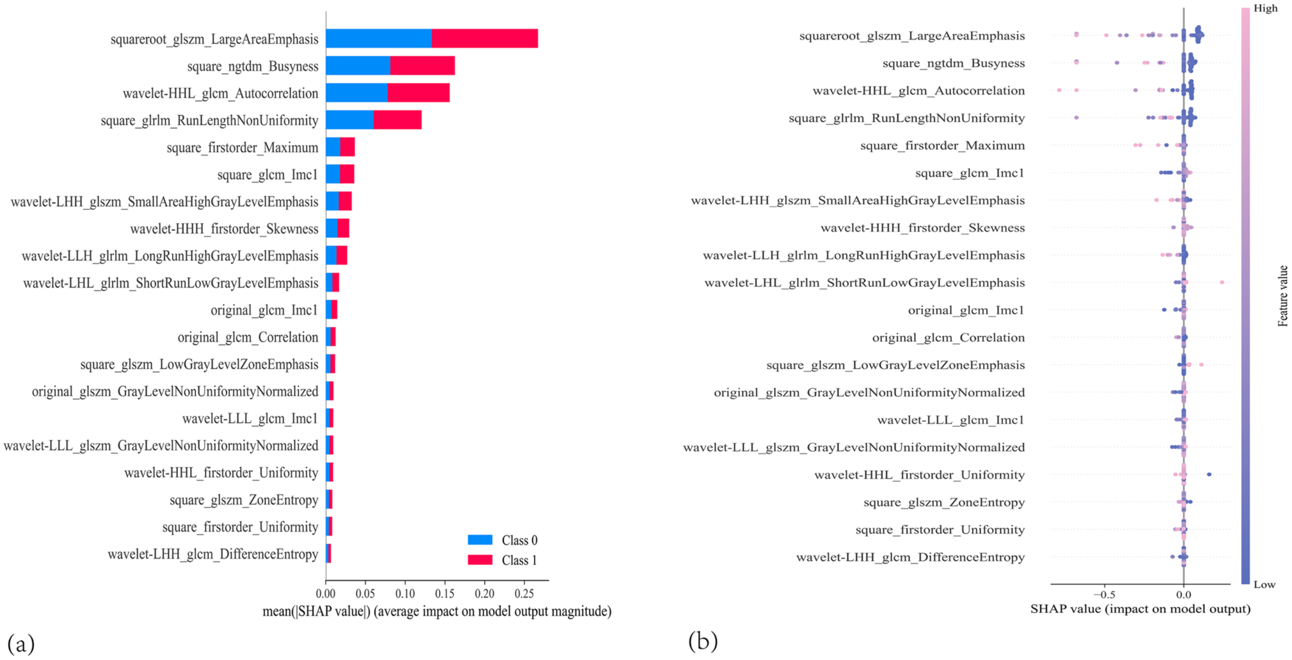

Fig. 10 **a** SHAP bar summary plot of the radiomic features in the integrated model. **b** SHAP dot summary plot of the radiomic features in the integrated model. The x-axis represents the SHAP values that describe the impact of each feature on model prediction. Positive SHAP values indicate an increased risk of PNI, whereas negative SHAP values indicate a decreased risk

Conclusion

Preoperative contrast-enhanced CT radiomics models hold significant clinical value in predicting the PNI status of pancreatic cancer patients. By integrating imaging and clinical data, our nomogram provides a noninvasive tool for risk stratification, prognosis evaluation, and personalized treatment planning. This approach not only complements traditional histopathology but also paves the way for precision oncology in pancreatic cancer management.

Abbreviations

PNI	Perineural invasion
EPNI	Extrapancreatic perineural invasion
ROI	Regions of interest
PDAC	Pancreatic ductal adenocarcinoma
CECT	Contrast-enhanced computed tomography
LR	Logistic regression
DT	Decision tree
RF	Random forest
GNB	Gaussian naive Bayes
SHAP	SHapley Additive exPlanations

Supplementary Information

The online version contains supplementary material available at https://doi.org/10.1186/s12885-025-14806-5.

Supplementary Material 1: Figure S1. (a) Non-PNI in PC. (b)PNI in PC

Acknowledgements

Not applicable.

Authors' contributions

Yuan Sun, Jiangyu Wang designed the study. Yuan Sun, Ming Li, Yan Li, and Tao Hu performed data analysis. Yuan Sun and Yan Li drafted the manuscript. Jiangyu Wang revised the manuscript. All authors read and approved the final manuscript.

Funding

Not applicable.

Data availability

The original contributions presented in the study are included in the article material, further inquiries can be directed to the corresponding author.

Declarations

Ethics approval and consent to participate

This study was approved by the Ethics Committee of The First Affiliated Hospital of Chongqing Medical University (Ethics Approval Number: 2025-375-01). The need for informed consent was waived for this study by the Ethics Committee of The First Affiliated Hospital of Chongqing Medical University, Chongqing, China, due to its retrospective design and irreversible anonymization of all data (Number :2025-375-01).

Consent for publication

We confirm that all authors of the manuscript agreed to publication.

Competing interests

The authors declare no competing interests.

Author details

[1]Department of Hepatobiliary Surgery, The First Affiliated Hospital of Chongqing Medical University, Chongqing, China

Received: 10 June 2025 / Accepted: 4 August 2025

References

1. Klein AP. Pancreatic cancer epidemiology: Understanding the role of lifestyle and inherited risk factors. Nat Rev Gastroenterol Hepatol. 2021;18(7):493–502. https://doi.org/10.1038/s41575-021-00457-x.
2. Mukund A, Afridi MA, Karolak A, Park MA, Permuth JB, Rasool G. Pancreatic ductal adenocarcinoma (PDAC): A review of recent advancements enabled by artificial intelligence. Cancers (Basel). 2024;16(12):2240. https://doi.org/10.3390/cancers16122240. Published 2024 Jun 17.
3. Principe DR, Underwood PW, Korc M, Trevino JG, Munshi HG, Rana A. The Current Treatment Paradigm for Pancreatic Ductal Adenocarcinoma and Barriers to Therapeutic Efficacy. Front Oncol. 2021;11:688377. Published 2021 Jul 15. https://doi.org/10.3389/fonc.2021.688377
4. Stathis A, Moore MJ. Advanced pancreatic carcinoma: current treatment and future challenges. Nat Rev Clin Oncol. 2010;7(3):163–72. https://doi.org/10.1038/nrclinonc.2009.236.
5. Liu B, Lu KY. Neural invasion in pancreatic carcinoma. Hepatobiliary Pancreat Dis Int. 2002;1(3):469–76.
6. Ceyhan GO, Demir IE, Altintas B, et al. Neural invasion in pancreatic cancer: a mutual tropism between neurons and cancer cells. Biochem Biophys Res Commun. 2008;374(3):442–7. https://doi.org/10.1016/j.bbrc.2008.07.035.
7. Demir IE, Ceyhan GO, Liebl F, D'Haese JG, Maak M, Friess H. Neural invasion in pancreatic cancer: the past, present and future. Cancers (Basel). 2010;2(3):1513–27. https://doi.org/10.3390/cancers2031513. Published 2010 Jul 14.
8. Torer N, Kayaselcuk F, Nursal TZ, et al. Adhesion molecules as prognostic markers in pancreatic adenocarcinoma. J Surg Oncol. 2007;96(5):419–23. https://doi.org/10.1002/jso.20654.
9. Lebe B, Sağol O, Ulukuş C, et al. The importance of Cyclin D1 and Ki67 expression on the biological behavior of pancreatic adenocarcinomas. Pathol Res Pract. 2004;200(5):389–96. https://doi.org/10.1016/j.prp.2004.02.010.
10. Li J, Kang R, Tang D. Cellular and molecular mechanisms of perineural invasion of pancreatic ductal adenocarcinoma. Cancer Commun (Lond). 2021;41(8):642–60. https://doi.org/10.1002/cac2.12188.
11. Huang C, Li Y, Guo Y, et al. MMP1/PAR1/SP/NK1R paracrine loop modulates early perineural invasion of pancreatic cancer cells. Theranostics. 2018;8(11):3074–86. https://doi.org/10.7150/thno.24281. Published 2018 Apr 30.
12. Chen JW, Bhandari M, Astill DS, et al. Predicting patient survival after pancreaticoduodenectomy for malignancy: histopathological criteria based on perineural infiltration and lymphovascular invasion. HPB (Oxford). 2010;12(2):101–8. https://doi.org/10.1111/j.1477-2574.2009.00140.x.
13. Zhou W, Jin W, Wang D et al. Laparoscopic versus open pancreaticoduodenectomy for pancreatic ductal adenocarcinoma: a propensity score matching analysis. Cancer Commun (Lond). 2019;39(1):66. Published 2019 Oct 28. https://doi.org/10.1186/s40880-019-0410-8
14. Demir IE, Friess H, Ceyhan GO. Neural plasticity in pancreatitis and pancreatic cancer. Nat Rev Gastroenterol Hepatol. 2015;12(11):649–59. https://doi.org/10.1038/nrgastro.2015.166.
15. Borhani AA, Dewan R, Furlan A, et al. Assessment of response to neoadjuvant therapy using CT texture analysis in patients with resectable and borderline resectable pancreatic ductal adenocarcinoma. AJR Am J Roentgenol. 2020;214(2):362–9. https://doi.org/10.2214/AJR.19.21152.
16. Khristenko E, Shrainer I, Setdikova G, Palkina O, Sinitsyn V, Lyadov V. Preoperative CT-based detection of extrapancreatic perineural invasion in pancreatic cancer. Sci Rep. 2021;11(1):1800. https://doi.org/10.1038/s41598-021-81322-4. Published 2021 Jan 19.
17. Gillies RJ, Kinahan PE, Hricak H. Radiomics: images are more than pictures, they are data. Radiology. 2016;278(2):563–77. https://doi.org/10.1148/radiol.2015151169.
18. Liu Z, Luo C, Chen X, Feng Y, Feng J, Zhang R, Ouyang F, Li X, Tan Z, Deng L, Chen Y, Cai Z, Zhang X, Liu J, Liu W, Guo B, Hu Q. Noninvasive prediction of perineural invasion in intrahepatic cholangiocarcinoma by clinicoradiological features and computed tomography radiomics based on interpretable machine learning: a multicenter cohort study. Int J Surg. 2024;110(2):1039–51. https://doi.org/10.1097/JS9.0000000000000881. PMID: 37924497; PMCID: PMC10871628.
19. Zou W, Wu D, Wu Y, et al. Nomogram predicts risk of perineural invasion based on serum biomarkers for pancreatic cancer. BMC Gastroenterol. 2023;23(1):315. https://doi.org/10.1186/s12876-023-02819-y. Published 2023 Sep 18.
20. Sarac M, Mravik M, Jovanovic D, Strumberger I, Zivkovic M, Bacanin N. Intelligent diagnosis of coronavirus with computed tomography images using a deep learning model. J Electron Imaging. 2023;32(2):021406–021406.
21. Prakash S, Kumar MV, Ran RS, Zivkovic M, Bacanin N, Antonijevic M. (2022). Hybrid GLFIL enhancement and encoder animal migration classification for breast cancer detection. Comput Syst Sci Eng, *41*(2).
22. Bezdan T, Milosevic S, Zivkovic KV, Bacanin M, N., Strumberger I. (2021). Optimizing Convolutional Neural Network by Hybridized Elephant Herding Optimization Algorithm for Magnetic Resonance Image Classification of Glioma Brain Tumor Grade. In 2021 Zooming Innovation in Consumer Technologies Conference (ZINC) (pp. 171–176). 2021 Zooming Innovation in Consumer Technologies Conference (ZINC). IEEE. https://doi.org/10.1109/zinc52049.2021.9499297
23. Zivkovic M, Bacanin N, Antonijevic M, Nikolic B, Kvascev G, Marjanovic M, Savanovic N. Hybrid CNN and XGBoost model tuned by modified arithmetic optimization algorithm for COVID-19 early diagnostics from X-ray images. Electronics. 2022;11(22):3798.
24. Grossberg AJ, Chu LC, Deig CR, et al. Multidisciplinary standards of care and recent progress in pancreatic ductal adenocarcinoma. CA Cancer J Clin. 2020;70(5):375–403. https://doi.org/10.3322/caac.21626.
25. Fu N, Fu W, Chen H, et al. A deep-learning radiomics-based lymph node metastasis predictive model for pancreatic cancer: a diagnostic study. Int J Surg. 2023;109(8):2196–203. https://doi.org/10.1097/JS9.0000000000000469. Published 2023 Aug 1.
26. Lee JH, Shin J, Min JH et al. Preoperative prediction of early recurrence in resectable pancreatic cancer integrating clinical, radiologic, and CT radiomics features. Cancer Imaging. 2024;24(1):6. Published 2024 Jan 8. https://doi.org/10.1186/s40644-024-00653-3
27. Zhao B, Xia C, Xia T, et al. Development of a radiomics-based model to predict occult liver metastases of pancreatic ductal adenocarcinoma: a multicenter study. Int J Surg. 2024;110(2):740–9. https://doi.org/10.1097/JS9.0000000000000908. Published 2024 Feb 1.
28. Fouquet T, Germain A, Brunaud L, Bresler L, Ayav A. Is perineural invasion more accurate than other factors to predict early recurrence after pancreatoduodenectomy for pancreatic head adenocarcinoma? World J Surg. 2014;38(8):2132–7. https://doi.org/10.1007/s00268-014-2465-7.
29. Deshmukh SD, Willmann JK, Jeffrey RB. Pathways of extrapancreatic perineural invasion by pancreatic adenocarcinoma: evaluation with 3D volume-rendered MDCT imaging. AJR Am J Roentgenol. 2010;194(3):668–74. https://doi.org/10.2214/AJR.09.3285.
30. Wang PH, Song N, Shi LB, Zhang QH, Chen ZY. The relationship between multiple clinicopathological features and nerve invasion in pancreatic cancer. Hepatobiliary Pancreat Dis Int. 2013;12(5):546 – 51. https://doi.org/10.1016/s1499-3872(13)60086-7. PMID: 24103287.
31. Tomlinson DR, Gardiner NJ. Glucose neurotoxicity. Nat Rev Neurosci. 2008;9(1):36–45. https://doi.org/10.1038/nrn2294. PMID: 18094705.
32. Zochodne DW. Diabetes mellitus and the peripheral nervous system: manifestations and mechanisms. Muscle Nerve. 2007;36(2):144 – 66. https://doi.org/10.1002/mus.20785. PMID: 17469109.
33. Giovannucci E, Michaud D. The role of obesity and related metabolic disturbances in cancers of the colon, prostate, and pancreas. Gastroenterology. 2007;132(6):2208-25. https://doi.org/10.1053/j.gastro.2007.03.050. PMID: 17498513.
34. Li J, Ma Q, Liu H, Guo K, Li F, Li W, Han L, Wang F, Wu E. Relationship between neural alteration and perineural invasion in pancreatic cancer patients with hyperglycemia. PLoS ONE. 2011;6(2):e17385. https://doi.org/10.1371/journal.pone.0017385. PMID: 21386984; PMCID: PMC3046240.
35. Karmazanovsky G, Gruzdev I, Tikhonova V, Kondratyev E, Revishvili A. Computed tomography-based radiomics approach in pancreatic tumors characterization. Radiol Med Published Online August. 2021;12. https://doi.org/10.1007/s11547-021-01405-0.
36. O'Connor JP, Rose CJ, Waterton JC, Carano RA, Parker GJ, Jackson A. Imaging intratumor heterogeneity: role in therapy response, resistance, and clinical outcome. Clin Cancer Res. 2015;21(2):249–57. https://doi.org/10.1158/1078-0432.CCR-14-0990.
37. Granata V, Grassi R, Fusco R, et al. Pancreatic cancer detection and characterization: state of the Art and radiomics. Eur Rev Med Pharmacol Sci. 2021;25(10):3684–99. https://doi.org/10.26355/eurrev_202105_25935.
38. Cheng K, Pan J, Liu Q, et al. Exosomal LncRNA XIST promotes perineural invasion of pancreatic cancer cells via miR-211-5p/GDNF. Oncogene. 2024;43(18):1341–52. https://doi.org/10.1038/s41388-024-02994-6.
39. Yang MW, Tao LY, Jiang YS, et al. Perineural invasion reprograms the immune microenvironment through cholinergic signaling in pancreatic ductal adenocarcinoma. Cancer Res. 2020;80(10):1991–2003. https://doi.org/10.1158/0008-5472.CAN-19-2689.

40. Guo X, Gao S, Yu J, Zhou Y, Gao C, Hao J. The imaging features of extrapancreatic perineural invasion (EPNI) in pancreatic cancer: A comparative retrospective study. Pancreatology. 2021;21(8):1516–23. https://doi.org/10.1016/j.pan.2021.08.010.
41. Chang ST, Jeffrey RB, Patel BN, et al. Preoperative multidetector CT diagnosis of extrapancreatic perineural or duodenal invasion is associated with reduced postoperative survival after pancreaticoduodenectomy for pancreatic adenocarcinoma: preliminary experience and implications for patient care. Radiology. 2016;281(3):816–25. https://doi.org/10.1148/radiol.2016152790.
42. Patel BN, Giacomini C, Jeffrey RB, Willmann JK, Olcott E. Three-dimensional volume-rendered multidetector CT imaging of the posterior inferior pancreaticoduodenal artery: its anatomy and role in diagnosing extrapancreatic perineural invasion. Cancer Imaging. 2013;13(4):580–90. https://doi.org/10.1102/1470-7330.2013.0051. Published 2013 Dec 30.

Publisher’s note